Mössbauer and Electron Paramagnetic Resonance Studies of the Cytochrome *bf* Complex†

Volker Schünemann,‡ Alfred X. Trautwein,*,‡ Jürgen Illerhaus,§ and Wolfgang Haehnel§

Institut für Physik, Medizinische Universität Lübeck, Ratzeburger Allee 160, 23538 Lübeck, Germany, and Institut für Biologie II/Biochemie, Albert-Ludwigs-Universität Freiburg, Schänzlestrasse 1, 79104 Freiburg, Germany

Received January 13, 1999; Revised Manuscript Received April 29, 1999

ABSTRACT: The ^{57}Fe-enriched cytochrome *bf* complex has been isolated from hydrocultures of spinach. It has been studied at different redox states by optical, EPR, and Mössbauer spectroscopy. The Mössbauer spectrum of the native complex at 190 K with all iron centers in the oxidized state reveals the presence of four different iron sites: low-spin ferric iron in cytochrome *b* [with an isomer shift (δ) of 0.20 mm/s, a quadrupole splitting (ΔE_Q) of 1.77 mm/s, and a relative area of 40%], low-spin ferric iron of cytochrome *f* (δ = 0.26 mm/s, ΔE_Q = 1.90 mm/s, and a relative area of 20%), and two high-spin ferric iron sites of the Rieske iron−sulfur protein (ISP) with a bis-cysteine and a bis-histidine ligated iron (δ_1 = 0.15 mm/s, ΔE_{Q1} = 0.70 mm/s, and a relative area of 20%, and δ_2 = 0.25 mm/s, ΔE_{Q2} = 0.90 mm/s, and a relative area of 20%, respectively). EPR and magnetic Mössbauer measurements at low temperatures corroborate these results. A crystal-field analysis of the EPR data and of the magnetic Mössbauer data yields estimates for the **g**-tensors (g_z, g_y, and g_x) of cytochrome *b* (3.60, 1.35, and 1.1) and of cytochrome *f* (3.51, 1.69, and 0.9). Addition of ascorbate reduces not only the iron of cytochrome *f* to the ferrous low-spin state (δ = 0.43 mm/s, ΔE_Q = 1.12 mm/s at 4.2 K) but also the bis-histidine coordinated iron of the Rieske 2Fe−2S center to the ferrous high-spin state (δ_2 = 0.73 mm/s, ΔE_{Q2} = −2.95 mm/s at 4.2 K). At this redox step, the Mössbauer parameters of cytochrome *b* have not changed, indicating that the redox changes of cytochrome *f* and the Rieske protein did not change the first ligand sphere of the low-spin ferric iron in cytochrome *b*. Reduction with dithionite further reduces the two hemes of cytochrome *b* to the ferrous low-spin state (δ = 0.49 mm/s, ΔE_Q = 1.08 mm/s at 4.2 K). The spin Hamiltonian analysis of the magnetic Mössbauer spectra at 4.2 K yields hyperfine parameters of the reduced Rieske 2Fe−2S center in the cytochrome *bf* complex which are very similar to those reported for the Rieske center from *Thermus thermophilus* [Fee, J. A., Findling, K. L., Yoshida, T., et al. (1984) *J. Biol. Chem. 259*, 124−133].

The cytochrome *bf* complex functions in photosynthetic electron transport as plastoquinol:plastocyanin oxidoreductase between photosystem II and photosystem I (for recent reviews, see refs *1* and *2*). It is closely related to the homologous cytochrome bc_1 complex of photosynthetic bacteria (reviewed in ref *3*) and of respiratory organisms. The electron transfer through the complex is coupled to proton translocation across the membrane by a Q cycle in addition to that linked to the quinol oxidation (*4*) which contributes to the electrochemical gradient driving the synthesis of ATP. It comprises four redox centers bound to three of its subunits. Cytochrome *b* carries two noncovalently bound *b*-type hemes, cytochrome *f* a covalently bound *c*-type heme, and the Rieske iron−sulfur protein a 2Fe−2S center. Other subunits are subunit IV which is homologous to the C-terminal part of the mitochondrial cytochrome *b* (*5*) and three small subunits, PetG, PetM, and PetL, each with a predicted single transmembrane α-helix but unknown function (*6*, *7*).

For the cytochrome *bf* complex, the structure has not been determined at atomic resolution except for fragments of cytochrome *f* from turnip truncated at the C-terminus (*8*) and of the iron−sulfur protein truncated at the N-terminus (*9*). The structure of the cytochrome *f* fragment uncovered a unique ligation of the heme iron by a histidine and the amino group of the N-terminal tyrosine. The Rieske iron−sulfur protein (ISP) contains a 2Fe−2S cluster domain with a structure similiar to that of the analogous protein of mitochondria (*10*). The three-dimensional structures of the complete cytochrome bc_1 complex from bovine (*11*) and also from chicken heart mitochondria (*12*) have been determined recently which showed the position of the four iron-containing centers spaced at distances between 21 and 31 Å from their nearest neighbors. Details of the structure of cytochrome *b* and the ligation of the two heme groups between two histidine residues of tilted transmembrane helices oriented in parallel have been resolved. Structural information about the mechanism of the electron transfer in the cytochrome bc_1 complex has been found at high resolution which yields

† Support to W.H. by the Deutsche Forschungsgemeinschaft (SFB 388/A1) and by European Community Contract BIO2CT-930076 and to A.X.T. by the Deutsche Forschungsgemeinschaft is gratefully acknowledged.

* To whom correspondence should be addressed. Telephone: ++49-451-500 4200. Fax: ++49-451-500 4214. E-mail: trautwein@physik.mu-luebeck.de.

‡ Medizinische Universität Lübeck.

§ Albert-Ludwigs-Universität Freiburg.

10.1021/bi990080n CCC: $18.00
Published on Web 06/18/1999

a redox-state-dependent position of the Rieske iron−sulfur protein (*12*, *13*). This indicates that the subunit with the iron center at one end of its compact, rigid structure moves between cytochrome c_1 and the quinol binding site at cytochrome *b*. The highly resolved structure of the iron−sulfur protein (*10*) shows the coordination of the 2Fe−2S center by two cysteine and two histidine residues. These ligands had been suggested by a Mössbauer study of the Rieske protein isolated from the bacterium *Thermus thermophilus* (*14*). Although the Rieske iron−sulfur protein from chloroplasts does not have a strand of amino acids which is found to form an α-helix and a loop in the protein from bc_1 complexes (*15*), it is likely that in the cytochrome *bf* complex the transfer follows a similar mechanism. The midpoint redox potentials of the Rieske 2Fe−2S protein and cytochrome *f* of 320 (*16*) and 340−365 mV (*17*, *18*), respectively, are considerably more positive than that of the two *b* cytochromes, b_H and b_L, of −45 and −150 mV, respectively (*19*). Besides the characterization by their UV−vis spectra, it is EPR which has provided information about the heme groups (*20*−*22*) and the Rieske iron−sulfur center (*23*) in the intact complex. Binding of the inhibitors stigmatellin or 2-hydroxyquinones to the quinol oxidizing site (Q_o or Q_p) causes an increase in the redox potential of the Rieske center (*24*) and affects also the absorbance spectrum of cytochrome *b* (*1*). This provides evidence for a strong interaction of these redox centers in the intact complex, which may be missing in the isolated subunits. Link and Iwata (*15*) have proposed a direct interaction between stigmatellin and the ϵ-N of a histidine ligand of the Rieske center. Thus, details about the electronic structure of the redox centers may help in understanding this interaction, the coordinated reduction of cytochrome b_L and the Rieske 2Fe−2S center, and the Q cycle. With respect to the five different iron centers in all cytochrome *bf* and bc_1 complexes, Mössbauer spectroscopy appears to be a suitable method for studying the electronic properties of the redox centers. However, to our knowledge, it has been used neither with a respiratory cytochrome bc_1 nor with a photosynthetic *bf* complex except for the isolated Rieske protein from the bacterial dioxygenase of *T. thermophilus* (*14*) and a preliminary study of the cytochrome *bf* complex from spinach (*25*). A detailed theoretical analysis of Mössbauer and EPR spectra has been established in particular for heme (*26*−*28*) and FeS proteins (*29*). Our new data are based on EPR spectra recorded at different redox states and on Mössbauer spectra measured at different temperatures, in the presence of a weak or a strong magnetic field, and at different redox states. The data are compared when available with those of biomimetic model compounds and are analyzed with the aim of identifying different iron centers.

MATERIALS AND METHODS

Plant Material. Spinach, *Spinachia oleracea*, was grown in an aerated hydroculture which was illuminated for 14 h by white light at 20 °C (51 W m^{-2}; Osram power star HQI-E 400W DV apparatus), followed by a 10 h dark period at 16 °C. The growing medium contained 6 mM KNO_3, 4 mM $Ca(NO_3)_2$, 2 mM $MgSO_4$, 1 mM KH_2PO_4, 4 mM $MgCl_2$, and as trace elements 4.6 μM H_3BO_3, 9 μM $MnCl_3$, 0.75 μM $ZnSO_4$, 0.32 μM $CuSO_4$, and 0.12 μM Na_2MoO_4 plus iron. To minimize contamination by ^{56}Fe (<0.02 ppm as determined by atomic absorption), only ultrapure chemicals were used. Sixty milligrams of iron with 95% ^{57}Fe was dissolved in concentrated HCl/HNO_3 (1:1), dried, and dissolved in 20 mL of H_2O. From this stock solution, an aliquot was added to the growing medium, yielding a $^{57}Fe^{3+}$ concentration of 21 μM. The spinach leaves were harvested after about 6 weeks.

Isolation of the Intact Cytochrome bf Complex. The cytochrome *bf* complex was isolated from the spinach leaves essentially as described by Hurt and Hauska (*18*) using 30 mM octyl glucoside and 0.5% (m/v) cholate. The complex harvested from the sucrose gradient ultracentrifugation was concentrated by ultrafiltration through a membrane with a 100 kDa cutoff (YM100, Amicon) to a final concentration of about 0.4 mM. To remove sucrose, the solution was diluted with buffer by a factor of 20 and concentrated again by ultrafiltration. The complex was reduced by addition of either 20 mM ascorbate or 20 mM sodium dithionite. UV−vis spectra were recorded with a dual beam spectrophotometer (UV 2101-PC, Shimadzu). The concentration of the cytochrome *bf* complex was determined as described by Hope and Valente (*30*). Chlorophyll was assessed by acetone extraction (*31*). For each measurement, a fresh sample of the concentrated cytochrome *bf* complex has been split into aliquots of 200 and 400 μL which were transferred to an EPR tube and a Mössbauer sample cell, respectively, and then frozen. The activity of the complex (35−45 nM) was determined with 6 μM decylplastoquinone as the electron donor and 20 μM horse heart cytochrome *c* as the electron acceptor (*18*). For SDS−PAGE with a gradient of 10 to 15% acrylamide, we followed the procedure of Laemmli (*32*). Protein standards (Sigma) for the ranges of 2.5−17 and 14−66 kDa were used for SDS−PAGE, and MW GF-1000 was used for size-exclusion chromatography. Staining was performed with Coomassie Brilliant Blue G250 (Serva).

EPR Spectroscopy. EPR spectra were recorded with a conventional X-band spectrometer (Bruker 200D SRC) equipped with a He-flow cryostat (ESR 910, Oxford Instruments) in the temperature range of 1.8−20 K. The spectra are simulated according to the procedure given by Beinert and Albracht (*33*) using orientation-dependent Gaussian line shapes. Since the spectra are simulated in field space, the simulations should be regarded as approximations. The bis-histidine low-spin hemes form the most extreme case of *g* strain broadening, and the lowest *g* values cannot be determined from the EPR traces. For the simulations that are presented, we used the **g**-tensors estimated by the analysis of the magnetic Mössbauer data. Spin quantitations were performed by integration of simulated absorption spectra and by comparison with a 0.85 mM ferric low-spin myoglobin azide standard. The integrated areas were weighted with Aasa correction factors (*34*).

Mössbauer Spectroscopy. Mössbauer spectra were recorded using a conventional spectrometer in the constant acceleration mode. Isomer shifts are given relative to α-Fe at room temperature. The spectra obtained at 20 mT were measured in a He-bath cryostat (Oxford model MD 306) equipped with a pair of permanent magnets. Spectra obtained at 10 mT were measured in a continuous flow cryostat (Oxford model CF 506) also equipped with permanent magnets. For the high-field spectra (5.35 T), a cryostat equipped with a superconducting magnet was used (Oxford Instruments). Magnetically split spectra of paramagnetic

samples were simulated in the spin Hamiltonian approximation described below; otherwise, spectra were analyzed by least-squares fits using Lorentzian line shape.

Spin Hamiltonian Formalism. The Zeeman interaction of a spin $\vec{\mathbf{S}}$ with an applied field $\vec{\mathbf{B}}$, with $\bar{\mathbf{g}}$ representing the electronic **g**-tensor, is described by the Hamiltonian

$$\hat{H}_{\text{eff}} = \mu_{\text{B}}\vec{\mathbf{S}}\cdot\bar{\mathbf{g}}\cdot\vec{\mathbf{B}} \tag{1}$$

where μ_{B} is the Bohr magneton. The g values of a ferric low-spin ($S = {}^1/_2$) system deviate from the isotropic spin-only value of 2.0023 which is caused by spin−orbit interaction. The g values can be calculated in terms of the mixing coefficients a, b, and c of the Fe t_{2g} (d_{yz}, d_{xz}, and d_{xy}) atomic orbitals (*35*):

$$\begin{aligned} g_x &= 2[a^2 - (b+c)^2] \\ g_y &= 2[(a+c)^2 - b^2] \\ g_z &= 2[(a+b)^2 - c^2] \\ a^2 + b^2 + c^2 &= 1 \end{aligned} \tag{2}$$

Accordingly, the relative energies of the Fe t_{2g} orbitals and their tetragonal (Δ/λ) and rhombic (V/λ) splittings can be derived from the g values:

$$V/\lambda = E_{yz} - E_{xz} = \frac{g_x}{g_z + g_y} + \frac{g_y}{g_z - g_x} \tag{3}$$

$$\Delta/\lambda = E_{xz} - E_{xy} - {}^1/_2 V/\lambda = \frac{g_x}{g_z + g_y} + \frac{g_z}{g_y - g_x} - {}^1/_2 V/\lambda$$

Here we follow the convention that the heme normal is the z-axis (*36*); λ is the spin−orbit coupling constant. Magnetic Mössbauer spectra were simulated using eq 1 together with the nuclear Hamiltonian (*29*)

$$\hat{H}_{\text{N}} = \frac{eQV_{zz}}{4I(2I-1)}[3\hat{I}_z^2 - I(I+1) + \eta(\hat{I}_x^2 - \hat{I}_y^2)] - g_{\text{N}}m_{\text{N}}\cdot\vec{\mathbf{I}}\cdot\vec{\mathbf{B}} + \langle\vec{\mathbf{S}}\rangle\cdot\bar{\mathbf{A}}\cdot\vec{\mathbf{I}} \tag{4}$$

where I denotes the spin of the nuclear ground state or excited state, $\hat{I}_x$, $\hat{I}_y$, and $\hat{I}_z$ denote the components of the nuclear spin operator, Q is the nuclear quadrupole moment of the nuclear excited state, V_{zz} is the main component of the electric-field gradient (efg)[1] tensor, η [$=(V_{xx} - V_{yy})/V_{zz}$] is the asymmetry parameter of the efg, and g_{N} is the nuclear g factor. The hyperfine coupling tensor $\bar{\mathbf{A}}$ was calculated from the expression (*37*, *38*)

$$\begin{aligned} A_x &= -P[-4bc - (1+\kappa)(a^2 - b^2 - c^2) + {}^3/_7(a^2 - 3b^2 - 3c^2) + {}^6/_7 a(b+c)] \\ A_y &= P[-4ac - (1+\kappa)(b^2 - a^2 - c^2) + {}^3/_7(b^2 - 3a^2 - 3c^2) + {}^6/_7 b(a+c)] \\ A_z &= P[-4ab - (1+\kappa)(c^2 - a^2 - b^2) + {}^3/_7(c^2 - 3a^2 - 3b^2) + {}^6/_7 c(a+b)] \end{aligned} \tag{5}$$

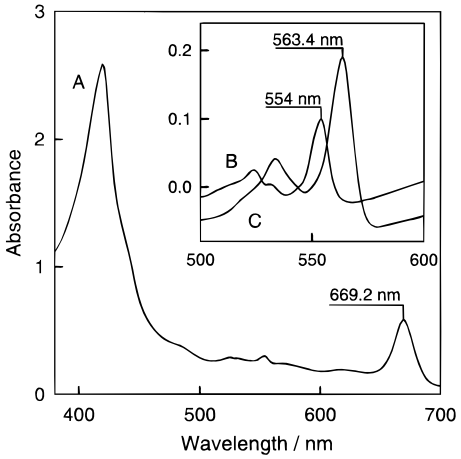

FIGURE 1: Representative optical spectra of the isolated cytochrome *bf* complex. (A) Spectrum of the isolated complex. (Inset) Difference spectra of (B) ascorbate-reduced minus ferricyanide-oxidized and (C) dithionite-reduced minus ascorbate-reduced.

Table 1: Optical and Enzymatic Characterization of the Mössbauer Samples[a]

sample	treatment	[cyt *f*] (μM)	[cyt *b*] (μM)	[chl] (μM)	[cyt *b*]/[cyt *f*]	[chl]/[cyt *f*]	activity (s^{-1})
1	untreated	450	880	673	1.95	1.5	8.0
2	ascorbate reduction	364	702.5	359	1.93	0.98	7.8
3	dithionite reduction	369	710	470	1.92	1.27	1.9

[a] The concentrations were determined before the activity after the Mössbauer measurements. Sample 1 was reduced with dithionite after thawing to give sample 3.

The constant P is taken to be −62 T and the Fermi contact constant κ to be 0.35 (*39*, *40*).

RESULTS

VIS Spectroscopy

The isolated cytochrome *bf* complex has been analyzed by size-exclusion chromatography with Sepharose 6B. The mass of 240 ± 20 kDa (data not shown) corresponds to the calculated mass of a dimeric complex of 230 kDa (*41*). Figure 1A shows the absorbance spectra of the complex harvested from the sucrose gradient. The maximum at 669.2 nm indicates about one chlorophyll molecule per monomeric complex as is found with most cytochrome *bf* complexes isolated from green plants (*1*, *41*). Attempts to remove this chlorophyll molecule have resulted in a decreased activity of the complex (not shown). The spectra labeled B and C in the inset of Figure 1 show the α-band region of the reduced minus oxidized difference spectrum of cytochrome *f* and cytochrome *b*, respectively. The spectra with the respective maximum at 554 and 563.4 nm of the α-band have been used to estimate the amounts of the cytochromes given in Table 1; the derived molar cytochrome *b*:cytochrome *f* ratios are close to 2:1. The values of the activity were measured after the Mössbauer measurements. Sample 3 results from

[1] Abbreviations: TMP, tetramesitylporphyrin; TPP, tetraphenylporphyrin; Py, pyridine; Im, imidazole; efg, electric field gradient; MCD, magnetic circular dichroism; Proto, protoporphyrin; cyt, cytochrome; chl, chlorophyll.

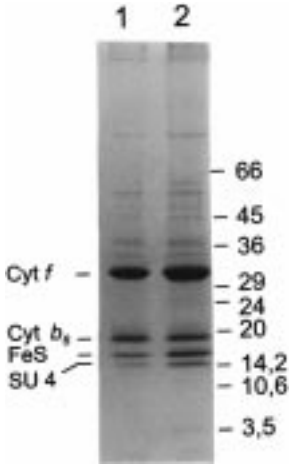

FIGURE 2: SDS−PAGE of the ^{57}Fe-containing *bf* complex from spinach on a 10 to 15% acrylamide gradient. For lanes 1 and 2, the same samples have been used as for the measurements of samples 1 and 2, respectively, given in Table 1. The positions of the molecular weight markers are indicated on the right and those of the four large subunits of the complex on the left. The gel was run with the samples after all Mössbauer experiments were completed.

reduction with dithionite after thawing of sample 1. Freezing and thawing of samples decreases the activity of the cytochrome *bf* complex considerably (*18*). Typical activity of fresh samples before freezing was >20 s^{-1} with cytochrome *c* as the electron acceptor which is in the line with the values reported previously (*3*, *42*, *43*). Stopped-flow experiments with the natural electron acceptor plastocyanin and the cytochrome *bf* complex isolated by the same procedure that was used for the Mössbauer samples exhibited a high second-order rate constant of 5×10^7 M^{-1} s^{-1} (J. Illerhaus and W. Haehnel, unpublished). Figure 2 shows the analysis of the samples on a gradient SDS−PAGE with the subunits well detected. The purification has not been extended to retain the highest activity of the ^{57}Fe-labeled complex. Faint bands indicate some contamination, which do not interfere with optical, EPR, or Mössbauer spectra.

EPR Spectroscopy

Cytochrome bf Complex in the Oxidized State. Figure 3a shows the EPR pattern of the native (oxidized) cytochrome *bf* complex at 20 K. The first-derivative trace is dominated by a low-field resonance at $g \sim 6$. The $g \sim 6$ resonance is characteristic for high-spin Fe(III) ($S = {}^5/_2$) in an axial ligand field and has been attributed previously to pentacoordinated ferric high-spin iron originating from those cytochrome *b* units which have lost an imidazole ligand during the preparation (*43*).

Spin quantitation of this signal yields a concentration of 0.024 mM which is minor compared to that of the concentrations of cytochrome *b* (0.32 mM) and of cytochrome *f* (0.16 mM), which have been determined by VIS spectroscopy. The resonance at $g = 3.5$ compares well with the g_z value reported for cytochrome *f* by previous EPR and magnetic circular dichroism (MCD) studies (3.51, 1.7, and <1.3) (*44*). Obviously, the g_z resonance of cytochrome *b* overlaps with that of cytochrome *f* which is observed at $g = 3.5$. The g_x and g_y values are not visible in the first-derivative trace of X-band EPR because of broad lines, a fact also observed in

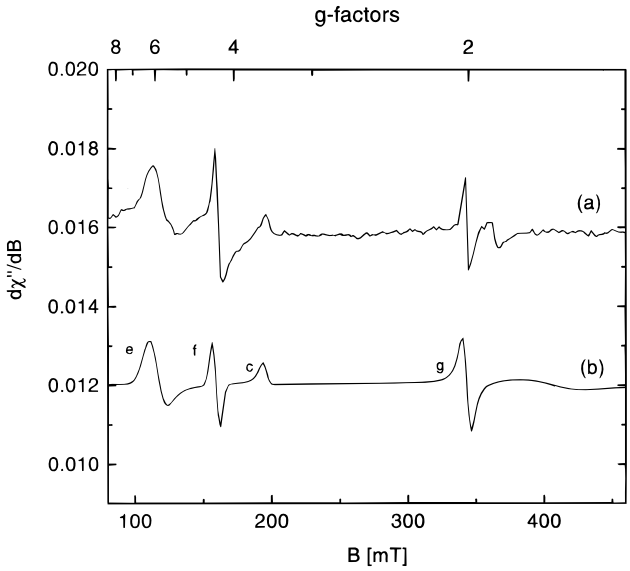

FIGURE 3: X-Band first-derivative EPR spectrum of the oxidized (^{56}Fe) cytochrome *bf* complex. (a) Experimental spectrum recorded at 20 K with a microwave power of 80 μW at 9.6456 GHz, a modulation amplitude of 0.5 mT, and a modulation frequency of 100 kHz. (b) Simulation obtained by taking the first derivative of the simulated X-band absorption EPR spectrum given in Figure 4b: (c) signal of cytochrome *f* with $\bar{\mathbf{g}} = (3.51, 1.69, 0.9)$ as estimated from the Mössbauer analysis, (e) ferric high-spin contamination with $\bar{\mathbf{g}} = (6.1, 5.9, 2.0)$, (f) ferric rhombic high-spin impurity with a *g* of 4.3, and (g) radical signal with a *g* of 2.003. The simulation contains also contribution d from cytochrome *b*, but due to its broad line shape in the absorption spectrum, it is not visible in the first-derivative spectrum. For the signal of cytochrome *b* and the relative intensities, see the simulations given in Figure 4 for the X-band absorption EPR spectrum.

cytochrome *b* of mammalian mitochondria (*45*). The extreme line broadening is demonstrated by an "absorption-like" spectrum (Figure 4a) which has been recorded under rapid-passage conditions in dispersion mode (*46*−*48*). We have used this technique to quantify (complementary to the Mössbauer analysis) the amounts of cytochrome *b* and of cytochrome *f* by spectral simulations presented below. The major absorption in this spectrum clearly extends from $g = 3-4$ down to 0.7, with a decline of intensity toward *g* values of $\ll 2$, as expected for extremely broadened lines due to **g**-strain. The low-field end of the spectrum is overlapping with the contribution from the $S = {}^5/_2$ species mentioned above which extends down to the $g = 2$ region only. The contribution from the $S = {}^5/_2$ species does not dominate the absorption trace as it does in the first-derivative trace. This becomes obvious from simulating the absorption pattern (Figure 4b) which, apart from a **g**-dependent correction factor (*34*), directly represents spectral intensities. With the **g**-tensors of cytochromes *f* and *b*, which have been taken from the Mössbauer analysis (vide infra) and assuming broad Gaussian line shapes, the subspectra shown in traces c and d of Figure 4 have been simulated, accounting for the major part of the absorption area of the measured spectrum (Figure 4a). Additional small spectral contributions arise from the high-spin Fe(III) species ($g \sim 6$; Figure 4e) and probably from an iron impurity ($g \sim 4.3$; Figure 4f) and a radical ($g \sim 2$; Figure 4g). The Aasa weighted relative contributions are 33% for cytochrome *f*, 62% for cytochrome *b*, 3% for the ferric high-spin species, 0.5% for the iron impurity, and

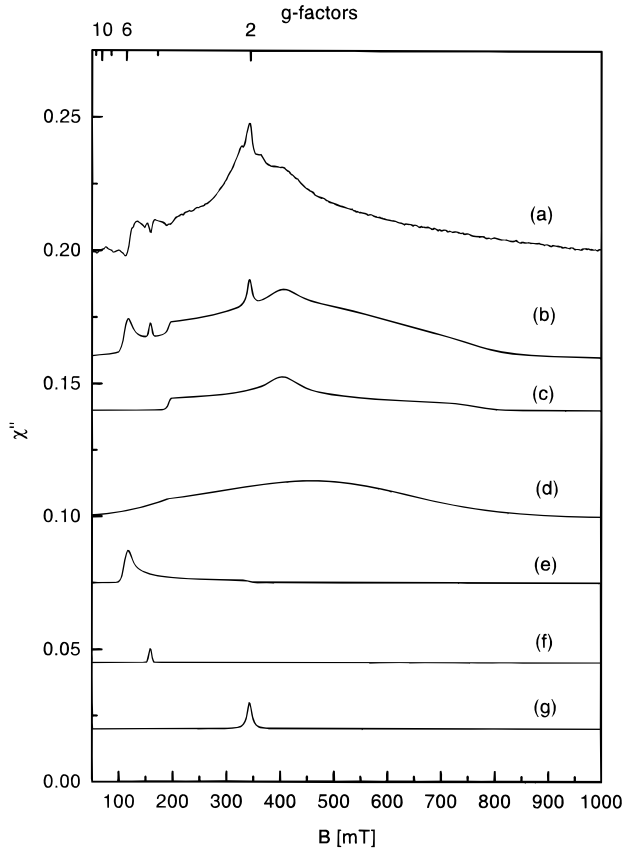

FIGURE 4: X-Band absorption EPR spectrum of the oxidized (^{56}Fe) cytochrome *bf* complex. (a) Recorded in dispersion mode at 1.8 K under rapid-passage conditions with a microwave power of 20 μW at 9.6437 GHz, a modulation frequency of 100 kHz, a modulation amplitude of 0.5 mT, and a sweep rate of 16.3 mT/s. (b) Superposition of the simulated traces: (c) simulation of cytochrome *f* with *g* values obtained from the Mössbauer analysis [$\bar{\mathbf{g}}$ = (3.51, 1.69, 0.9), 33% relative intensity], (d) simulation of cytochrome *b* with *g* values also obtained from the Mössbauer analysis [$\bar{\mathbf{g}}$ = (3.6, 1.35, 1.1), 62% relative intensity], (e) simulation of a ferric high-spin contamination with $\bar{\mathbf{g}}$ = (6.1, 5.9, 2.0) (3.0% relative intensity), (f) simulation of a ferric rhombic high-spin impurity with a *g* of 4.3 (0.5% relative intensity), and (g) simulation of a radical signal with a *g* of 2.003 (1.5% relative intensity). Integration of trace c yields 1.0 spin per cytochrome *f*, and integration of trace d yields 1.88 spins per cytochrome *b*.

1.5% for the radical species. Figure 4b represents the sum of the individual contributions from traces c−g of Figure 4 and compares well with the measured absorption spectrum (Figure 4a).

Cytochrome bf Complex Reduced by Ascorbate. The ascorbate-reduced cytochrome *bf* complex exhibits a first-derivative spectrum in which the intensity of the signal at $g = 3.5$ is significantly decreased (Figure 5a) compared to the corresponding spectrum of the oxidized complex (Figure 3a). Ascorbate reduces cytochrome *f* but not cytochrome *b* (*43*). Therefore, we relate the remaining very small $g = 3.6$ signal to cytochrome *b* (see the inset of Figure 5) (*43*). In the ascorbate-reduced complex, a new signal appeared with *g* values (2.03, 1.90, and 1.76) which agree with those reported for the Rieske center in the reduced state (*14*). A quantitative assignment of the various spectral species is again based on the analysis of the measured absorption pattern (Figure 6a). The Aasa-weighted relative contributions are 33% for the Rieske center (Figure 6c), 59% for cytochrome *b* (Figure 6d), 7% for the ferric high-spin species ($g \sim 6$; Figure 6e),

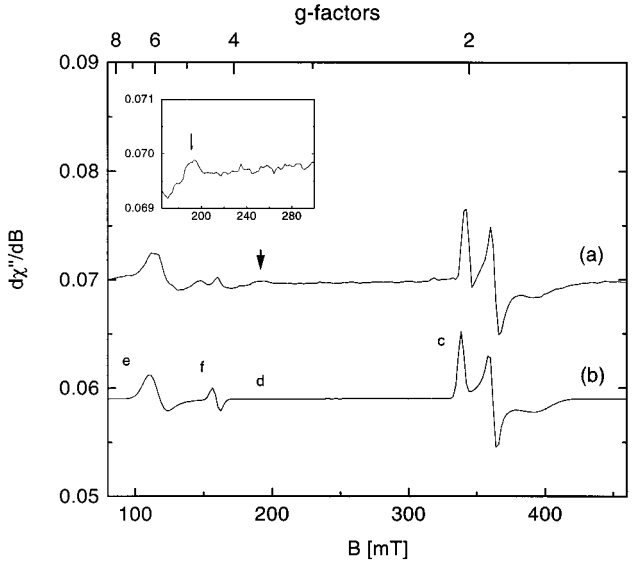

FIGURE 5: X-Band first-derivative EPR spectrum of the ascorbate-reduced (^{57}Fe) cytochrome *bf* complex. (a) Experimental spectrum recorded at 20 K (other parameters as described in the legend of Figure 3a). The inset shows the $g = 3.6$ signal originating from cytochrome *b*. (b) Simulation obtained by taking the first derivative of the simulated X-band absorption EPR spectrum given in Figure 6b: (c) contribution of the reduced Rieske center with $\bar{\mathbf{g}}$ = (2.027, 1.895, 1.76), (e) ferric high-spin contamination with $\bar{\mathbf{g}}$ = (6.1, 5.9, 2.9), and (f) ferric rhombic high-spin impurity with a *g* of 4.3. For the signal of cytochrome *b* and relative intensities, see the simulations given in Figure 6 for the X-band absorption EPR spectrum.

and 1% for an iron impurity ($g \sim 4.3$; Figure 6f). The sum of these individual contributions is represented by Figure 6b and compares well with the measured absorption spectrum (Figure 6a). However, we want to emphasize that the broad signal of cytochrome *b* is hardly visible in the first-derivative mode (Figure 5a). Therefore, we have used the **g**-tensor estimated by the analysis of the magnetic Mössbauer data [$\bar{\mathbf{g}}$ = (3, 6, 1.35, 1.1), vide infra] to simulate the contribution of cytochrome *b* (Figure 6d) to the spectrum, which has been recorded under rapid-passage conditions (Figure 6a). The amount of the ferric high-spin species ($g \sim 6$) turned out to be larger in the ascorbate-reduced cytochrome *bf* complex (7%) than in the oxidized complex (3%). This may be due to different batches, because the ascorbate-reduced complex originates from a ^{57}Fe-enriched preparation and the oxidized complex from a ^{56}Fe-containing preparation (with only natural abundance ^{57}Fe).

Cytochrome bf Complex Reduced by Dithionite. The dithionite-reduced cytochrome *bf* complex exhibits a first-derivative trace, which is solely due to the reduced Rieske center (data not shown). To verify that cytochrome *b* has been reduced to an EPR-invisible ferrous low-spin ($S = 0$) complex, a spectrum was also recorded under rapid-passage conditions; the latter exhibits a well-defined baseline with no other absorption pattern than that of the reduced Rieske center (data not shown).

Mössbauer Spectroscopy

Cytochrome bf Complex in the Oxidized State. Figure 7 shows the Mössbauer spectrum of the isolated cytochrome *bf* complex at 190 K.

(1) The doublet with an isomer shift δ of 0.20 mm/s and a quadrupole splitting ΔE_Q of 1.77 mm/s, characteristic for

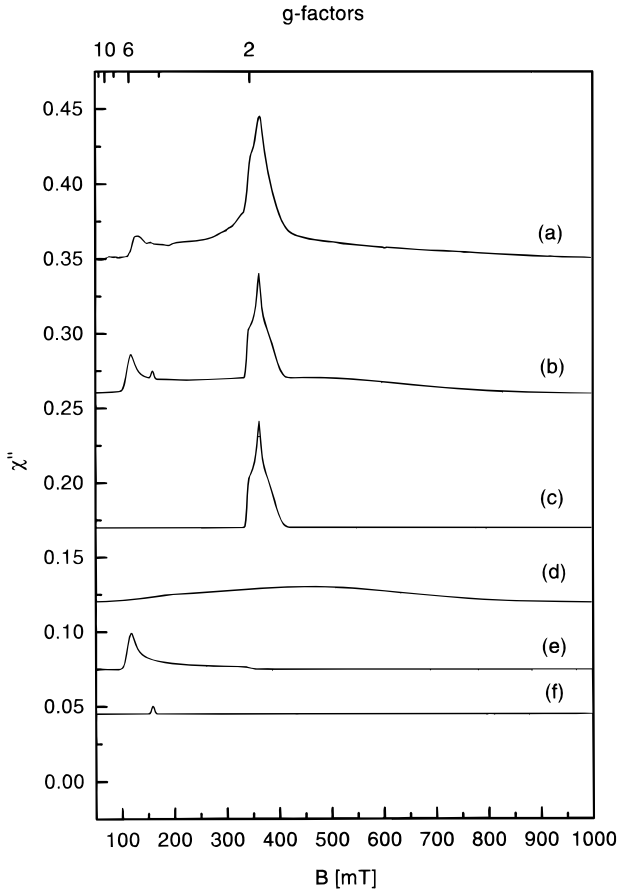

FIGURE 6: X-Band absorption EPR spectrum of the ascorbate-reduced (^{57}Fe) cytochrome *bf* complex. (a) Experimental spectrum recorded at 1.8 K (other parameters as described in the legend of Figure 4a). (b) Superposition of the simulated traces: (c) simulation of the reduced Rieske center with $\bar{\mathbf{g}} = (2.027, 1.895, 1.76)$ (33% relative intensity), (d) simulation of cytochrome *b* with *g* values obtained from the Mössbauer analysis [$\bar{\mathbf{g}} = (3.6, 1.35, 1.1)$, 59% relative intensity], (e) simulation of a ferric high-spin contamination with $\bar{\mathbf{g}} = (6.1, 5.9, 2.0)$ (7.0% relative intensity), and (f) simulation of a ferric rhombic high-spin impurity with a *g* of 4.3 (1% relative intensity).

ferric low-spin iron, exhibits 40% of the total absorption area and is attributed to the iron in cytochrome *b*. Comparing ΔE_Q with the corresponding values of model compounds (see Table 2) suggests that cytochrome *b* contains two histidines in the axial positions with the imidazoles oriented perpendicular to each other. The model complex [Fe(TMP)(4-$NMe_2Py)_2$]ClO_4 with a perpendicular orientation of pyridine ligands exhibits a quadrupole splitting similar to that of cytochrome *b*. Parallel alignment of the axial ligands would result in a significantly higher quadrupole splitting as shown for example by [Fe(Proto IX)$(HIm)_2$]Cl (*49*) and [Fe(TPP)-$(NH_2PzH_2)_2$]Cl (*50*) which both reveal ΔE_Q values of >2 mm/s (Table 2). We note that the quadrupole splittings of ferric low-spin porphyrin systems do depend on the type of axial ligation and also on deviations from planarity of the porphyrin. The ΔE_Q values in Table 2 indicate that this deviation of the porphyrins in cytochrome *b* and in [Fe-$(TMP)(4\text{-}NMePy)_2$]ClO_4 is of a similar size.

(2) The doublet with a δ of 0.29 mm/s and a ΔE_Q of 1.93 mm/s (20% of the total absorption area) also exhibits parameters typical for ferric low-spin iron and is therefore attributed to Fe in cytochrome *f*. Recent crystal structure data

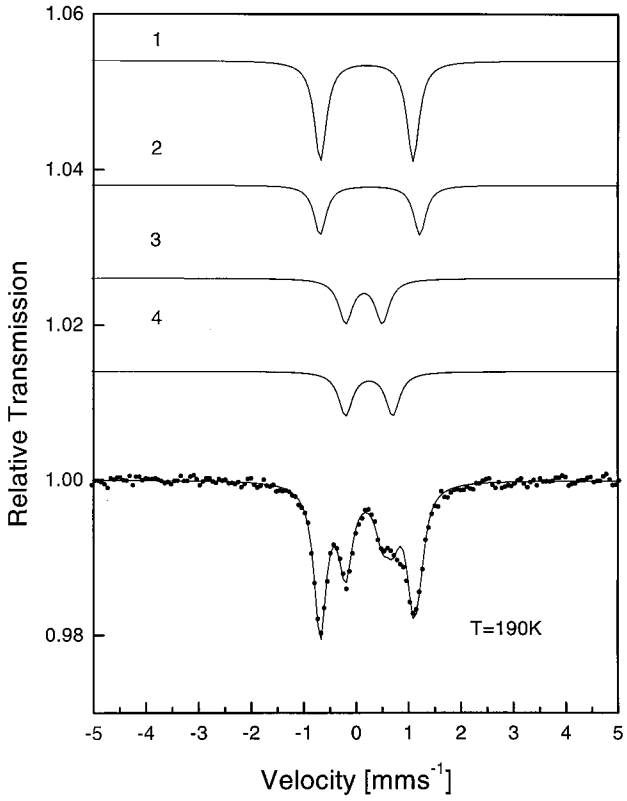

FIGURE 7: Mössbauer spectrum of the native (^{57}Fe) cytochrome *bf* complex recorded at 190 K. The solid line represents a fit with the parameters given in Table 3: (1) cytochrome *b*, (2) cytochrome *f*, and (3 and 4) Rieske center.

for cytochrome *f* have shown a mixed axial ligand structure, i.e., with histidine and the α-amino group of the N-terminal tyrosine (*8*).

(3 and 4) Two doublets with a δ of 0.15 mm/s and a ΔE_Q of 0.70 mm/s and with a δ of 0.25 mm/s and a ΔE_Q of 0.90 mm/s are discernible because the above-mentioned subspectra 1 and 2 are spectroscopically "separated" from spectra 3 and 4 in applied fields at 4.2 K (Figure 8a,b). The parameters of spectra 3 and 4 are very similar to those reported for the 2Fe−2S center of the oxidized Rieske iron−sulfur protein from *T. thermophilus* (*14*) and attributed to the bis-cysteine and bis-histidine ligated iron, respectively. The antiparallel coupling of the local $S = {}^5/_2$ iron spins in the Rieske center is indicated by zero magnetic splitting in a 10 mT field at 4.2 K (Figure 8a). Application of a 5.3 T field (perpendicular to the γ-ray) induces a nuclear Zeeman splitting which corresponds exactly to the applied field, confirming the diamagnetic ground state of the Rieske center (Figure 8b). Both cytochromes *f* and *b*, in the native complex, exhibit magnetic splitting at 10 mT and at 5.35 T (Figure 8a,b). As pointed out above (Materials and Methods), it is possible to calculate spectral parameters such as the **A**-tensor from the electronic *g* values. This method has been successfully used to evaluate magnetic Mössbauer spectra of the heme groups of nitrite reductase isolated from *Desulfovibrio desulfuricans* (*26*), of the tetraheme cytochrome c_3 from *Desulfovibrio baculatus* (*27*), and of *Paracoccus denitrificans* cytochrome *c* peroxidase (*51*).

In the present case, we made use of a g_z value of 3.51 and a g_y value of 1.7 for cytochrome *f* (*44*) and of a g_z value of 3.6 for cytochrome *b*. To minimize the free-parameter space,

Table 2: Mössbauer Parameters of Low-Spin Hemes and Corresponding Model Compounds

species	ΔE_Q (mm/s)	δ (mm/s)	T (K)	orientation of axial ligands	ref
cyt *f*	1.90	0.26	190	−	this work
cyt *b*	1.77	0.20	190	−	this work
$[Fe(TMP)(4\text{-}NMe_2Py)_2]ClO_4$	1.74	0.20	77	perpendicular	*40*
$[Fe(TPP)(Py)_2]Cl$	1.25	0.16	77	perpendicular	*40*
$[Fe(Proto\ IX)HIm)_2]Cl$	2.30	0.24	77	parallel	*49*
$[Fe(Proto\ IX)(Py)_2]Cl$	1.95	0.28	4.2	perpendicular	*56*
$[Fe(TPP)(NH_2PzH_2)_2]Cl$	2.50	0.25	4.2	parallel	*50*

Table 3: Mössbauer Parameters of the Native Cytochrome *bf* Complex[a]

subspectrum	T (K)	$\bar{\mathbf{g}}$	ΔE_Q (mm/s)	δ (mm/s)	Γ (mm/s)	η	β^b (deg)	$\bar{\mathbf{A}}/g_N\mu_N{}^c$ (T)	relative area (%)
cyt *b* (1)	190		1.77	0.20	0.32				40
cyt *f* (2)			1.90	0.26	0.32				20
Rieske (3)			0.70	0.15	0.28				20
Rieske (4)			0.90	0.25	0.28				20
cyt *b* (1)	4.2	1.1, 1.35, 3.60	1.77	0.30	0.30	0	0	−26.1, −4.0, 92.6	40
cyt *f* (2)		0.9, 1.69, 3.51	1.93	0.36	0.30	0	40	−31.5, 13.5, 85.4	20
Rieske (3)			0.70	0.25	0.32				20
Rieske (4)			0.90	0.35	0.32				20

[a] Isomer shifts and quadrupole splittings were obtained from the 190 K spectrum (Figure 7), and spin Hamiltonian parameters were obtained from simulating the 4.2 K spectra in applied fields of 10 mT perpendicular to γ and 5.35 T perpendicular to γ (Figure 8). [b] Euler angle between the axes system of the **A**-tensor and of the efg tensor. [c] Hyperfine-coupling tensor components.

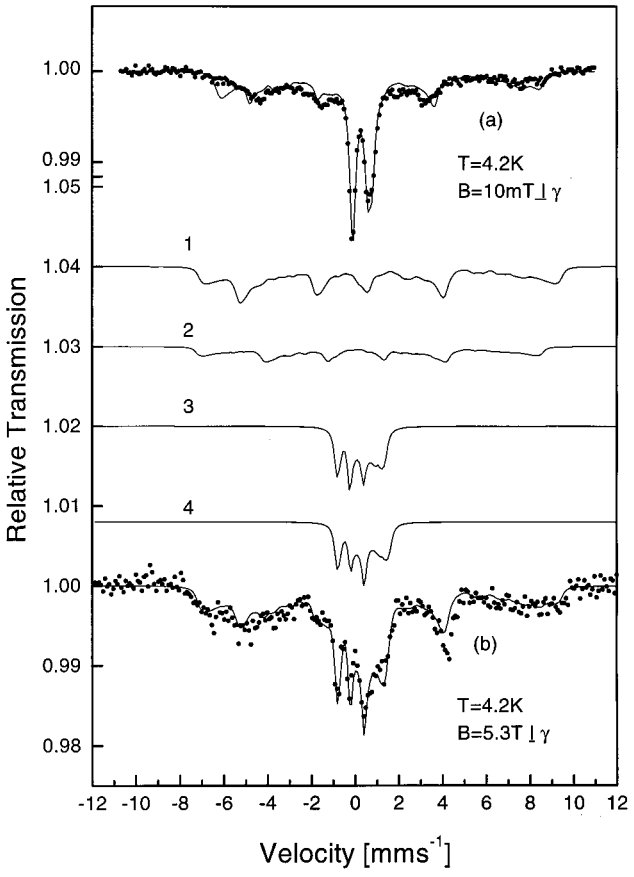

FIGURE 8: Mössbauer spectra of the native (^{57}Fe) cytochrome *bf* complex recorded at 4.2 K in a field of 10 mT perpendicular to γ (a) and 5.35 T perpendicular to γ (b). Solid lines are simulations with the parameters given in Table 3. The numbering of the subspectra is the same as in Figure 7.

we have additionally assumed $g_x^2 + g_y^2 + g_z^2 = 16$ (*28*, *35*). Thus, for cytochrome *b*, one free parameter (either g_x or g_y) remains for simulating the spectra, while for cytochrome *f*, the simulation is completely self-consistent. Figure 8b shows the simulation of the paramagnetic part originating from the two ferric low-spin cytochromes *f* and *b* with the parameter set summarized in Table 3.

(5) Part of the total absorption area (≤7%) is probably due to a spectrum which exhibits parameters of ferric high-spin iron ($S = {}^5/_2$), which is most likely due to pentacoordinated Fe(III) in cytochrome *b* (*43*) as discussed in the EPR section. We have not included a corresponding subspectrum in the analysis of the measured Mössbauer spectra of the native cytochrome *bf* complex because of unknown magnetic hyperfine parameters.

Cytochrome bf Complex Reduced by Ascorbate. Mössbauer spectra of the ascorbate-reduced complex were recorded at 190 K in zero field and at 4.2 K in small and in high applied fields (Figures 9 and 10). In a small field, a complicated magnetically split pattern together with a doublet is observed (Figure 10a). The parameters of the doublet are characteristic for low-spin Fe(II). This assignment of the doublet is confirmed by the high-field spectrum (trace 2 in Figure 10b). Hence, we conclude that cytochrome *f* has been reduced to the ferrous low-spin state ($S = 0$). The paramagnetic part of the magnetically split pattern contains the contributions of oxidized cytochrome *b* ($S = {}^1/_2$) and of the reduced Rieske center ($S_{tot} = {}^1/_2$). For the simulation of cytochrome *b* (trace 1 in Figure 10b), the same parameters have been used as in Figure 8, while for the simulation of the Rieske center (traces 3 and 4 in Figure 10b), the Mössbauer parameters of the Rieske center in *T. thermophilus* (*14*) have been used. The high-field spectrum at 4.2 K (Figure 10b and Table 4) was simulated with the same parameter set as the low-field spectrum at 4.2 K (Figure 10a) and the zero-field spectrum at 190 K (Figure 9). Small temperature effects in δ may be due to a second-order Doppler shift and in ΔE_Q (of the ferrous high-spin iron in the Rieske center) due to Boltzmann population of excited orbital states. In addition to the two cytochromes, *b* (trace 1) and *f* (trace 2), and to the Rieske center (traces 3 and 4), a small part of the total absorption area (≤7%) is probably due to a ferric high-spin iron, which we have not included in the analysis of the measured Mössbauer spectra of the ascorbate-reduced complex.

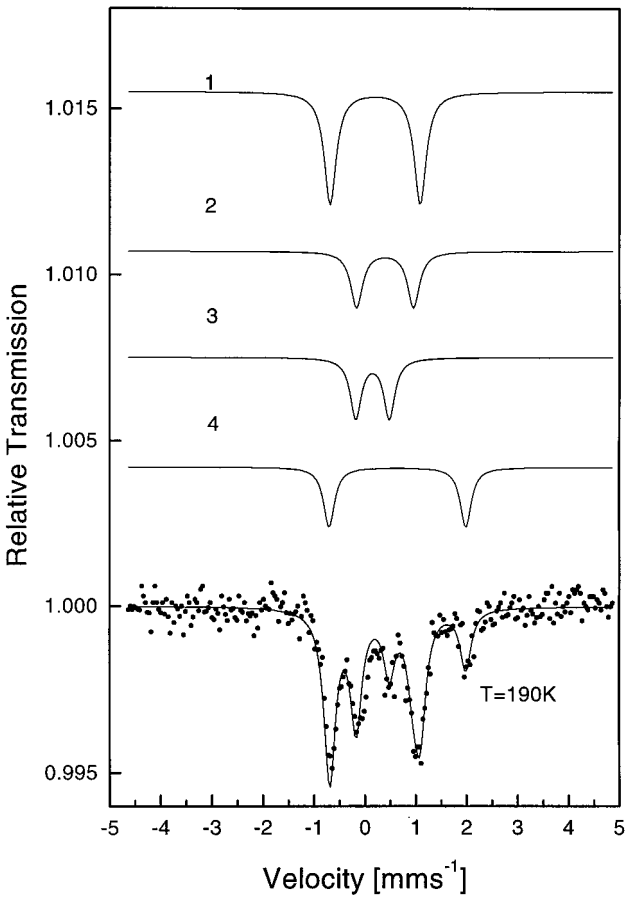

FIGURE 9: Mössbauer spectrum of the ascorbate-reduced (^{57}Fe) cytochrome *bf* complex recorded at 190 K. The solid line represents a fit with the parameters given in Table 4. The numbering of the subspectra is the same as in Figure 7.

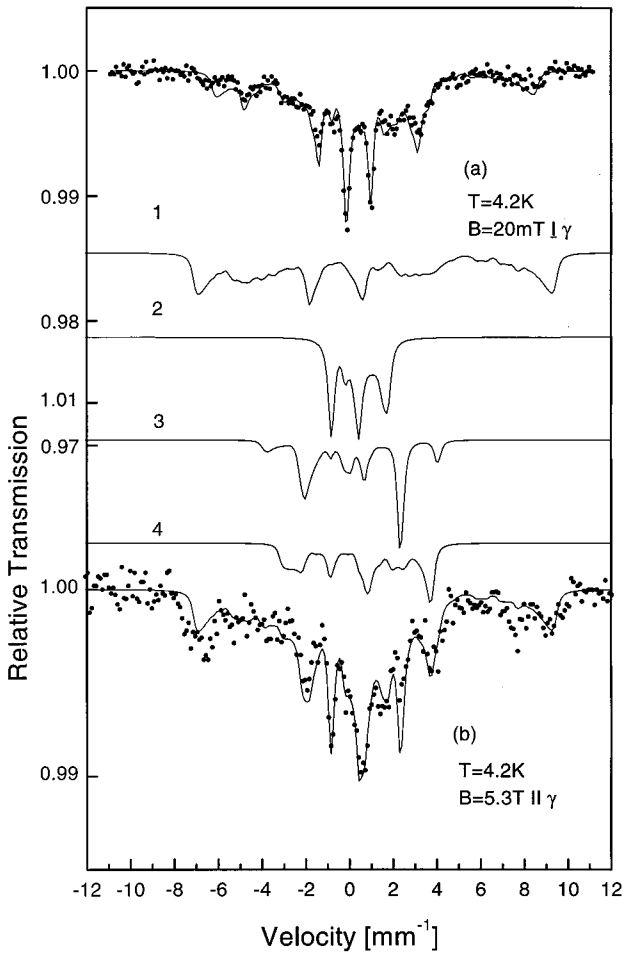

FIGURE 10: Mössbauer spectra of the ascorbate-reduced (^{57}Fe) cytochrome *bf* complex recorded at 4.2 K in a field of 20 mT perpendicular to γ (a) and 5.35 T parallel to γ (b). Solid lines are simulations with the parameters given in Table 4. The numbering of the subspectra is the same as in Figure 7.

Dithionite-Reduced Cytochrome bf Complex. Addition of dithionite reduces the iron in cytochrome *b*, which has remained in the ferric state after addition of ascorbate. The iron in cytochrome *b* changes from the ferric low-spin ($S = {}^1/_2$) to the ferrous low-spin state ($S = 0$). The latter (trace 1 in Figures 11 and 12) exhibits isomer shifts and quadrupole splittings comparable to the corresponding values of the ferrous low-spin iron in cytochrome *f* (Table 5). Furthermore, cytochrome *b* does not exhibit magnetic splitting in a small applied field at 4.2 K (trace 1 in Figure 12), which is an additional indication of the above-mentioned change of the spin state. The Mössbauer parameters of the iron sites in cytochrome *f* and the Rieske center (traces 2−4 in Figures 11 and 12, and Table 5) exhibit no significant difference in the presence of ascorbate or dithionite. The iron which has been attributed to a pentacoordinated site in cytochrome *b* changes during dithionite treatment from the ferric high-spin ($S = {}^5/_2$) to the ferrous high-spin state ($S = 2$). The isomer shifts and quadrupole splittings of the latter, measured at 190 and 4.2 K (trace 5 in Figures 11 and 12, and Table 5), are indeed very similar to the corresponding values of pentacoordinated deoxymyoglobin (*52*).

DISCUSSION

The objective of this work has been to study the electronic structure of the five iron centers in the intact cytochrome *bf*

Table 4: Mössbauer Parameters of the Cytochrome *bf* Complex after Addition of Ascorbate[a]

subspectrum	T (K)	$\bar{\mathbf{g}}$	ΔE_Q (mm/s)	δ (mm/s)	Γ (mm/s)	η	β (deg)	$\bar{\mathbf{A}}/g_N\mu_N$ (T)	relative area (%)
cyt *b* (1)	190		1.77	0.20	0.28				40
cyt *f* (2)			1.12	0.40	0.28				20
Rieske (3)			0.66	0.15	0.28				20
Rieske (4)			2.69	0.64	0.28				20
cyt *b* (1)	4.2	1.1, 1.35, 3.60	1.77	0.30	0.30	0	0	−26.2, −4.0, 92.6	40
cyt *f* (2)			1.12	0.43	0.30	0			20
Rieske (3)		1.76, 1.9, 2.03	0.70	0.25	0.25	0	0	−40.3, −36.7, −31.5	20
Rieske (4)		1.76, 1.9, 2.03	−2.95	0.73	0.25	−3	0	8.0, 10.2, 24.2	20

[a] Isomer shifts and quadrupole splittings were obtained from the 190 K spectrum (Figure 9), and spin Hamiltonian parameters were obtained from simulating the 4.2 K spectra in applied fields of 20 mT perpendicular to γ and 5.35 T parallel to γ (Figure 10). The **A**-tensor and the asymmetry parameter η of the two iron sites of the reduced Rieske center are the same as those reported for the Rieske center of *T. thermophilus* (*14*).

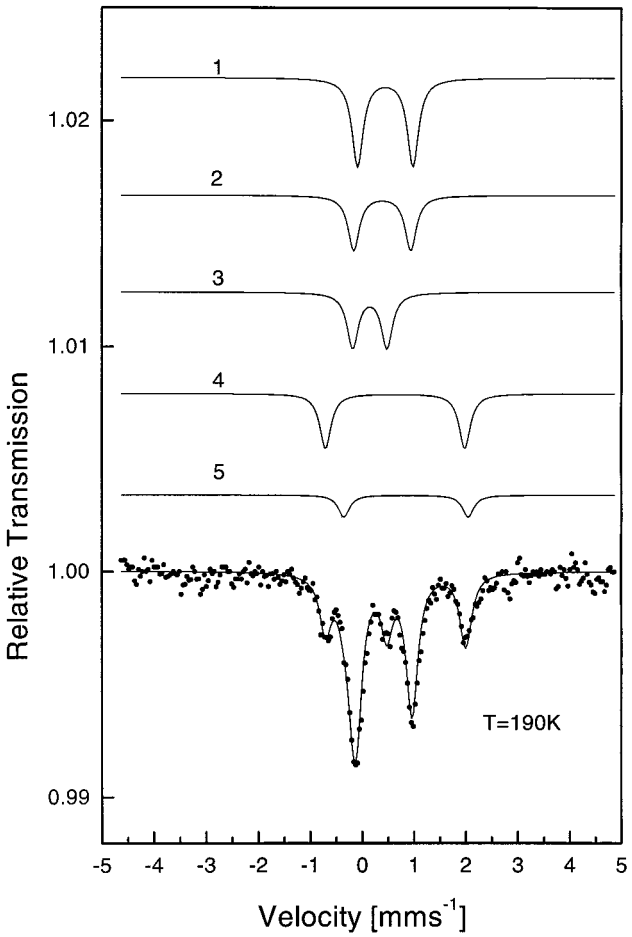

FIGURE 11: Mössbauer spectrum of the dithionite-reduced (^{57}Fe) cytochrome *bf* complex recorded at 190 K. The solid line represents a fit with the parameters given in Table 5. The numbering (1−4) of the subspectra is the same as in Figure 7. Spectrum 5 represents data for a ferrous high-spin site which probably corresponds to five-coordinated iron in cytochrome *b* as discussed in the text.

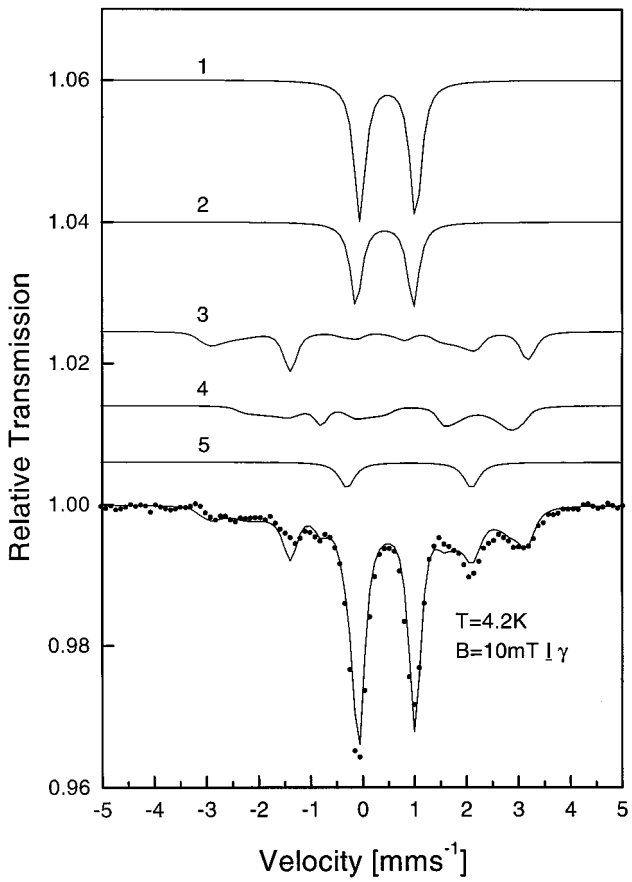

FIGURE 12: Mössbauer spectrum of the dithionite-reduced (^{57}Fe) cytochrome *bf* complex recorded at 4.2 K in a field of 10 mT perpendicular to γ. The solid line is a simulation with the parameters given in Table 5. The numbering (1−5) of the subspectra is the same as in Figure 11.

complex from spinach chloroplasts by EPR and under a wide variety of experimental conditions in Mössbauer experiments.

EPR of the oxidized cytochrome *bf* complex in the first-derivative mode indicates strongly broadened signals due to **g**-strain. However, simulations of EPR spectra recorded under rapid-passage conditions clearly indicate the presence of ferric low-spin iron sites in both cytochromes, *f* and *b*, in the expected molar ratio of 1:2. Optical characterization confirms this result (Table 1).

Mössbauer measurements at elevated temperatures (Figure 7, 9, and 11) indicate the presence of four different iron sites in the intact complex: the iron sites of cytochrome *b* and cytochrome *f* [low-spin ($S = {}^1/_2$) in the oxidized as well as in the reduced form ($S = 0$)] and the two iron sites of the Rieske center [high-spin ($S = {}^5/_2$) in the oxidized form and high-spin with localized mixed valencies in the reduced form ($S = {}^5/_2$ and $S = 2$, respectively)]. The EPR analysis yields an additional minor ferric high-spin species in the oxidized and ascorbate-reduced form. The Mössbauer analysis of the dithionite-reduced state yields a minor ferrous high-spin species. Its isomer shift ($\delta = 0.90$ mm/s) indicates penta-coordinated Fe(II) (*52*). This confirms the assignment (*43*) that the heme iron of a minor part of cytochrome *b*, i.e., 9% of the total cytochrome *b*, has lost one axial histidine ligand even during the preparation with a minimized loss of activity.

Table 5: Mössbauer Parameters of the Cytochrome *bf* Complex after Addition of Dithionite[a]

subspectrum	T (K)	$\bar{\mathbf{g}}$	ΔE_Q (mm/s)	δ (mm/s)	Γ (mm/s)	η	β (deg)	$\bar{\mathbf{A}}/g_N\mu_N$ (T)	relative area (%)
cyt *b* (1)	190		1.07	0.45	0.26	.			32
cyt *f* (2)			1.10	0.39	0.26				20
Rieske (3)			0.66	0.15	0.26				20
Rieske (4)			2.69	0.64	0.26				20
Fe(II) (5)			2.40	0.90	0.28				8
cyt *b* (1)	4.2		1.08	0.49	0.26				32
cyt *f* (2)			1.10	0.43	0.26				20
Rieske (3)		1.76, 1.9, 2.03	0.70	0.25	0.25	0	0	−40.3, −36.7, −31.5	20
Rieske (4)		1.76, 1.9, 2.03	−2.95	0.43	0.25	−3	0	8.0, 10.2, 24.2	20
Fe(II) (5)			2.40	0.90	0.35				8

[a] Isomer shifts and quadrupole splittings were obtained from the 190 K spectrum (Figure 11). The spin Hamiltonian parameters deduced from Figure 12 for the reduced Rieske center are identical to those obatined from Figure 10.

The high- and low-potential forms of the two iron centers in cytochrome *b* have yielded experimental Mössbauer spectra which we have simulated with the same parameter set for both centers under all the conditions that were applied. However, due to the limitation in the signal-to-noise ratio of the measured magnetic hyperfine patterns (it took about 2 weeks to collect one spectrum, and samples with higher concentrations could not be prepared), we cannot exclude slightly different **A**-tensor components for the two cytochromes *b*.

Recently, Walker (*53*) compared Mössbauer and EPR features of low-spin ferriheme centers, in which the axial ligands are in perpendicular planes (type I) or in approximately parallel planes (type II). Type I centers exhibit large g_z values of 3.4−3.6, ΔE_Q values in the range of 1.2−1.8 mm/s, and very large A_{zz} (80−100 T). In the case of type II centers, g_z is somewhat smaller, corresponding to a smaller A_{zz} (40−66 T), and ΔE_Q is larger (2.1−2.4 mm/s) than for type I. The parameters observed in our study for cytochromes *b* and *f* are very similar to those reported for type I centers, while those found for cytochrome *c* (*54*), where the methionine dominates the ligand effects, are close to type II parameters.

Mössbauer measurements at 4.2 K in small and high fields, applied parallel and perpendicular to the γ-ray, yielded magnetically disturbed line shapes (Figure 8, 10, and 12) which have been simulated on the basis of the crystal-field approach of Oosterhuis and Lang (*37*) with the parameter sets presented in Tables 3−5. This analysis includes the **g**-tensors of the ferric low-spin iron sites in the native cytochrome *b* (3.60, 1.35, 1.1) and of the native cytochrome *f* (3.51, 1.69, 0.9). These values yield, according to eq 3, the tetragonal (Δ/λ) and rhombic (V/λ) orbital splittings for cytochrome *b* ($\Delta/\lambda = 14.2$, and $V/\lambda = 0.76$) and cytochrome *f* ($\Delta/\lambda = 4.2$, and $V/\lambda = 0.82$).

The Mössbauer parameters of iron in cytochrome *b* in the native ferric state are the same as after reduction of cytochrome *f* and of the Rieske center by ascorbate. This leads to the conclusion that the first ligand sphere of the low-spin ferric iron in cytochrome *b* does not change upon the reduction of both the cytochrome *f* and the Rieske center. Therefore, the redox (and net charge) changes of cytochrome *f* and the Rieske protein do not change the standard redox potential of the cytochrome *b*.

The two iron sites of the Rieske center exibit very similar isomer shifts and quadrupole splittings compared to those reported for the Rieske center from *T. thermophilus*, in both the native and reduced state (*14*) (compare $\delta_1 = 0.24$ mm/s, $\Delta E_{Q1} = 0.52$ mm/s, $\delta_2 = 0.32$ mm/s, and $\Delta E_{Q2} = 0.91$ mm/s for the oxidized Rieske center and $\delta_1 = 0.31$ mm/s, $\Delta E_{Q1} = 0.63$ mm/s, $\delta_2 = 0.74$ mm/s, and $\Delta E_{Q2} = -3.05$ mm/s for the reduced Rieske center from ref *14* with the parameters given in Tables 3−5). Also, the hyperfine parameters of the Rieske center from the toluene-4-monoxygenase of *Pseudomonas mendocina* (*55*) are very similiar to those of the Rieske center in the cytochrome *bf* complex. This remarkable result includes also the simulation of the magnetic Mössbauer spectra of the reduced Rieske center (Figures 10 and 12), for which the same spin Hamiltonian parameters have been used that were used for the Rieske center from *T. thermophilus* (*14*). The striking similarity of the electronic properties of the Rieske centers in the cytochrome *bf* complex, of the Rieske protein from *T. thermophilus*, and from the toluene-4-monoxygenase of *P. mendocina* leads to the conclusion that the overall binding geometry around the iron is the same in these and possibly in other Rieske centers as well as in those of mitochondria. The three-dimensional structure of the latter has been determined recently at high resolution (*10*).

ACKNOWLEDGMENT

We are grateful to Christoph Gelhaus for running the gels.

REFERENCES

1. Hauska, G., Schütz, M., and Büttner, M. (1996) in *Oxygenic Photosynthesis: The Light Reactions* (Ort, D. R., and Yocum, C. F., Eds.) pp 377−398, Kluwer Academic Publishers, Dordrecht, The Netherlands.
2. Kallas, T. (1994) in *The Molecular Biology of Cyanobacteria* (Bryant, D. A., Ed.) pp 259−317, Kluwer Academic Publishers, Dordrecht, The Netherlands.
3. Hauska, G. (1986) *Methods Enzymol. 126*, 271−285.
4. Mitchell, P. (1975) *FEBS Lett. 56*, 1−6.
5. Widger, W. R., Cramer, W. A., Herrmann, R., and Trebst, A. (1984) *Proc. Natl. Acad. Sci. U.S.A. 81*, 674−678.
6. Schmidt, C. L., and Malkin, R. (1993) *Photosynth. Res. 38*, 73−81.
7. Pierre, Y., and Popot, J.-L. (1993) *C. R. Acad. Sci., Ser. III 316*, 1404−1409.
8. Martinez, S. E., Huang, D., Szczepaniak, A., Cramer, W. A., and Smith, J. L. (1994) *Structure 2*, 95−105.
9. Carell, C. J., Zang, H., Cramer, W. A., and Smith, J. L. (1997) *Structure 5*, 1613−1626.
10. Iwata, S., Saynovits, M., Link, T. A., and Michel, H. (1996) *Structure 4*, 567−579.
11. Iwata, S., Lee, J. W., Okada, K., Lee, J. K., Iwata, M., Rasmussen, B., Link, T. A., Ramaswamy, S., and Jap, B. K. (1998) *Science 281*, 64−71.
12. Zhang, Z., Huang, L., Shulmeister, V. M., Chi, Y.-I., Kim, K. K., Hung, L.-W., Crofts, A. R., Berry, E. A., and Kim, S.-H. (1998) *Nature 392*, 677−684.
13. Yu, C.-A., Xia, D., Kim, H., Deisenhofer, J., Zhang, L., Kachurin, A. M., and Yu, L. (1998) *Biochim. Biophys. Acta 1365*, 151−158.
14. Fee, J. A., Findling, K. L., Yoshida, T., Hille, R., Tarr, G. E., Hearshen, D. O., Dunham, W. R., Day, E. P., Kent, T. A., and Münck, E. (1984) *J. Biol. Chem. 259*, 124−133.
15. Link, T. A., and Iwata, S. (1996) *Biochim. Biophys. Acta 1275*, 54−60.
16. Riedel, A., Rutherford, A. W., Hauska, G., Müller, A., and Nitschke, W. (1991) *J. Biol. Chem. 266*, 17838−17844.
17. Davenport, H. E., and Hill, R. (1952) *Proc. R. Soc. London, Ser. B 139*, 327−345.
18. Hurt, E., and Hauska, G. (1982) *J. Bioenerg. Biomembr. 14*, 405−424.
19. Kramer, D. M., and Crofts, A. R. (1994) *Biochim. Biophys. Acta 1184*, 193−201.
20. Salerno, J. C., McGill, J. W., and Gerstle, G. C. (1983) *FEBS Lett. 162*, 257−261.
21. Rigby, S. E. J., Moore, G. R., Gray, J. C., Gadsby, P. M. A., George, S. J., and Thomson, A. J. (1988) *Biochem. J. 256*, 571−577.
22. Nitschke, W., Hauska, G., and Rutherford, A. W. (1989) *Biochim. Biophys. Acta 974*, 223−226.
23. Malkin, R., and Posner, H. B. (1978) *Biochim. Biophys. Acta 501*, 552−554.
24. von Jagow, G., and Onishi, T. (1985) *FEBS Lett. 185*, 311−315.
25. Illerhaus, J., Sanakis, Y., Petrouleas, V., and Haehnel, W. (1995) in *Photosynthesis: from Light to Biosphere* (Mathis, P., Ed.) Vol. II, pp 551−554, Kluwer Academic Publishers, Dordrecht, The Netherlands.

26. Costa, C., Moura, J. J. G., Moura, I., Liu, M. Y., Peck, H. D., Jr., LeGall, J., Wang, Y., and Huynh, B. H. (1990) *J. Biol. Chem. 265*, 14382−14387.
27. Ravi, N., Moura, I., Costa, C., Teixeira, M., LeGall, J., and Moura, J. J. G. (1992*) Eur. J. Biochem. 204*, 779−782.
28. Debrunner, P. G. (1993) in *Biological Magnetic Resonance, Volume 13: EMR of Paramagnetic Molecules* (Berliner, L. J., and Reuben, J., Eds.) pp 59−101, Plenum Press, New York.
29. Trautwein, A. X., Bill, E., Bominaar, E. L., and Winkler, H. (1991*) Struct. Bonding (Berlin) 78*, 1−95.
30. Hope, A. P., and Valente, P. (1996) *Photosynth. Res. 49*, 37−48.
31. Porra, R. J., Thompson, W. A., and Kriedemann, P. E. (1989) *Biochim. Biophys. Acta 975*, 384−394.
32. Laemmli, U. K. (1970) *Nature 227*, 680−685.
33. Beinert, H., and Albracht, S. (1982) *Biochim. Biophys. Acta 683*, 245−277.
34. Aasa, R., and Vånngard, T. (1975) *J. Magn. Reson. 19*, 308−315.
35. Griffith, J. S. (1956) *Proc. R. Soc. London, Ser. A 235*, 23−36.
36. Taylor, C. P. S. (1977) *Biochim. Biophys. Acta 491*, 137−149.
37. Oosterhuis, W. T., and Lang, G. (1969) *J. Chem. Phys. 50*, 4381−4387.
38. Oosterhuis, W. T., and Lang, G. (1969) *Phys. Rev. 178* (2), 439−456.
39. Lang, G. (1970) *Q. Rev. Biophys. 3*, 1−60.
40. Safo, M. K., Gupta, G. P., Walker, F. A., and Scheidt, W. R. (1988) *J. Am. Chem. Soc. 110*, 1207−1215.
41. Huang, D., Everly, R. M., Cheng, R. H., Heymann, J. B., Schägger, H., Sled, V., Ohnishi, T., Baker, T. S., and Cramer, W. A. (1994) *Biochemistry 33*, 4401−4409.
42. Black, M. T., Widger, W. R., and Cramer, W. A. (1987) *Arch. Biochem. Biophys. 252*, 655−661.
43. Nitschke, W., and Hauska, G. (1987) *Biochim. Biophys. Acta 892*, 314−319.
44. Rigby, S. E. J., Moore, G. R., Gray, J. C., Gadsby, P. M. A., George, S. J., and Thomson, A. J. (1988) *Biochem. J. 256*, 571−577.
45. Beinert, H. (1978) in *Methods of Enzymology* (Fleischer, S., and Packer, L., Eds.) Vol. LIV, pp 133−150, Academic Press, San Diego, CA.
46. Benecky, M., Frew, J. E., Scowen, N., Jones, P., and Hoffman, B. M. (1993) *Biochemistry 32*, 11929−11933.
47. Schulz, C. E., Rutter, R., Sage, J. T., Debrunner, P. G., and Hager, L. P. (1984*) Biochemistry 23*, 4743−4754.
48. Rutter, R., Hager, L. P., Dhonau, H., Hendrich, M., Valentine, M., and Debrunner, P. (1984) *Biochemistry 23*, 6809−6816.
49. Epstein, L. M., Straub, D. K., and Maricondi, C. (1967) *Inorg. Chem. 6*, 1720−1724.
50. Schünemann, V., Benda, R., Trautwein, A. X., Raitsimring, A., and Walker, F. A. (1999) *JBIC, J. Biol. Inorg. Chem.* (submitted for publication).
51. Prazeres, S., Moura, J. J. G., Moura, I., Gilmour, R., Goodhew, C. F., Pettigrew, G. W., Ravi, N., and Huynh, B. H. (1995) *J. Biol. Chem. 270*, 24264−24269.
52. Trautwein, A. X., and Harris, F. E. (1975) *Theor. Chim. Acta 38*, 65−69.
53. Walker, F. A. (1999) *Coord. Chem. Rev.* (in press).
54. Dwivedi, A., Toscano, W. A., and Debrunner, P. G. (1979) *Biochim. Biophys. Acta 576*, 502−508.
55. Pikus, J. D., Studts, J. M., Achim, C., Kauffmann, K. E., Münck, E., Steffan, R. J., McClay, K., and Fox, B. G. (1996) *Biochemistry 35*, 9106−9119.
56. Rhynaid, D., Lang, G., Spartalian, K., and Yonetani, T. (1979) *J. Chem. Phys. 71* (9), 3715−3721.

BI990080N